ARTICLE OPEN

Check for updates

Highly efficient fiber-shaped organic solar cells toward wearable flexible electronics

Dan Lv[1,2,3], Qianqing Jiang[2,3], Yuanyuan Shang[4]✉ and Dianyi Liu[1,2,3]✉

Fiber-shaped solar cells (FSCs) show great potential to act as the power source in the wearable electronics field. Due to the unique advantages of the fiber-shaped organic solar cells (FOSCs), such as all-solid-state, ease of fabrication, and environmental friendliness, FOSCs are the strongest candidate among all types of FSCs for wearable electronics. However, the development of FOSCs is seriously lagging behind other types of FSCs. In this work, we demonstrate the efficient FOSCs with non-fullerene-acceptors (NFAs)-based light-harvesting materials. The FOSCs present efficiencies exceeding 9% under AM 1.5 G irradiation conditions. The performance influence factors including hole/electron transport layers, active layer, counter electrodes, solvents, and especially, the environmental humidity is systematically studied. The FOSCs not only can easily drive the electrical devices but also can be woven into the textile to charge the smartwatch. The study exhibits the great potential to apply the FOSCs as the power supply source in the wearable electronic field.

npj Flexible Electronics (2022)6:38 ; https://doi.org/10.1038/s41528-022-00172-w

INTRODUCTION

Flexible fiber-shaped solar cells (FSCs) can not only supply electrical power but also easy to be weaved into clothing and textiles, which makes them promising candidates for the energy supply of wearable electronic devices[1,2]. The various types of FSCs including fiber-shaped dye-sensitized solar cells (FDSSCs)[3,4], fiber-shaped organic solar cells (FOSCs)[5–7], and fiber-shaped perovskite solar cells (FPSCs)[8–10] have made dramatic progress during the past years. Much efforts have been devoted to improve the performance of the FSCs, including developing new photovoltaic materials and optimizing the device structures[11,12]. Especially, the efficiencies of F-DSSCs and F-PSCs are promoted to over 10%[13,14]. The increased efficiency indicates that the FSCs can meet more energy consumption requirements for electrical applications.

Compared with the FDSSC and FPSC, the efficiency of the FOSC is still low and it stays at ~ 2% which has not any improvement in the past ten years[6,7,15]. However, the FOSC is still one of the most promising candidates for the development of power suppliers on wearable electronic devices because of its unique advantages, such as all-solid-state, ease of fabrication, environmental friendliness, and satisfying material stability. In particular, FOSC has already been successfully fabricated into the organic photovoltaic textile which provides a good instance for the application of FPSC in the wearable electronics field[16].

The performance of FOSC is highly dependent on the performance of organic semiconductors. Most of the previously reported FOSCs adopt organic semiconductor blends with polymer-based donors and fullerene-based acceptors as the light absorption materials, such as P3HT:$PC_{61}BM$, and PTB7:$PC_{71}BM$[6,7,15,16]. Since the light absorption ranges of the traditional active layers are generally limited in the visible light range (< 700 nm), the efficiencies of fullerene-based organic photovoltaics (OPVs) are hard to exceed 10%, which also limits the performance of fullerene-based FOSCs. The non-fullerene acceptor (NFA) materials develop rapidly in recent years which greatly promote the development of OPVs[17–19]. The absorption range of NFA molecules can be extended to over 1000 nm, as the result, the efficiencies of NFA-based planar-structured OPVs are significantly improved to over 18%[20,21]. Similar to the fullerene-based acceptors, NFA materials are also solution processible and easy to deposit on the plane and flexible substrates. To date, the NFA-based organic semiconductors have not been introduced into FSCs yet.

According to the results from previous studies, the NFA-based photovoltaic materials are expected to break through the efficiency bottleneck if they can be used as the active layer materials in FOSCs. Aim to solve the low-efficiency problem of FOSCs, we introduced the NFA-based organic semiconductors as the light-harvesting materials in this work. In addition, the low-cost industrial stainless-steel wire is used as the substrate and the core electrode. Carbon nanotube (CNT) yarn or silver wire is used as the counter electrode to twine around the primary electrode. A solution-processed perylene diimide derivative interlayer material is used as the electron transfer layer. The prepared FOSCs can achieve an efficiency of up to 9.40% under AM 1.5 G standard irradiation conditions. The performance influence factors including hole/electron transport layers, counter electrodes, and fullerene additive are systematically studied. Especially, the dependence of device performance on environmental humidity is observed by recording the device photovoltaic parameters during the study period, and the mechanisms of the humidity influences are carefully investigated. By connecting in series or parallel, the highly efficient flexible FOSCs exhibit the robust performance to drive the small electrical device. Particularly, the FOSCs can be successfully woven into the watchband to charge the smartwatch. The initial attempt on charging smart devices indicates the great potential of FOSCs to be applied in practical wearable electronics.

[1]Zhejiang University, Hangzhou, Zhejiang Province, China. [2]Key Laboratory of 3D Micro/nano Fabrication and Characterization of Zhejiang Province, School of Engineering, Westlake University, Hangzhou, Zhejiang Province, China. [3]Institute of Advanced Technology, Westlake Institute for Advanced Study, Hangzhou, Zhejiang Province, China. [4]School of Physics and Microelectronics, Zhengzhou University, Zhengzhou, Henan Province, China. ✉email: yuanyuanshang@zzu.edu.cn; liudianyi@westlake.edu.cn

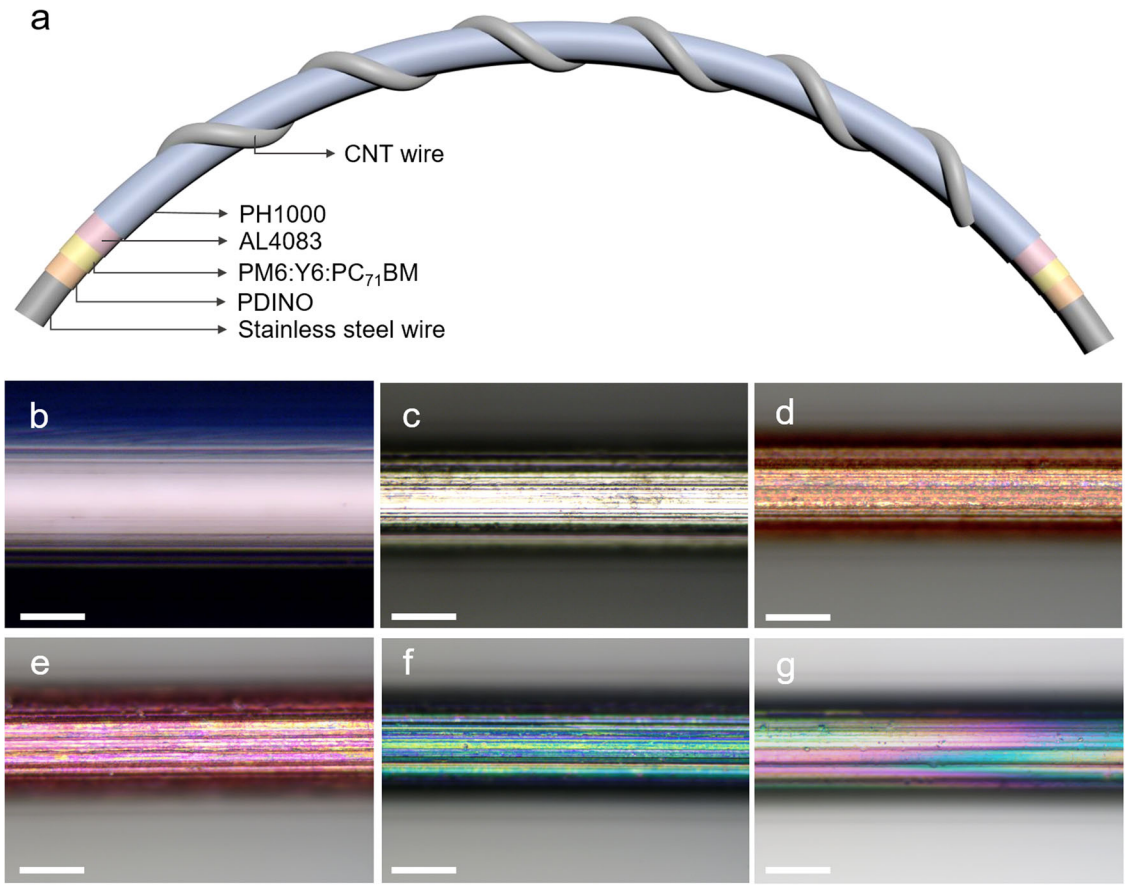

Fig. 1 Depiction of the FOSCs with architecture schematic and optical microscopic images. a Illustration of the fiber-shaped organic solar cell (FOSC). Optical micrographs of **b** lab-grade stainless-steel wire (∅ = 0.127 mm); **c** primary industry-grade stainless-steel wire electrode (∅ = 0.10 mm); **d** PDINO ETL; **e** PM6:Y6:$PC_{71}BM$ active layer; **f** AL4083 layer; and **g** PH1000 layer. The scale bar is 50 μm.

RESULTS AND DISSCUSSION

Device fabrication of FOSCs

In order to reduce the instability of manual operation in previous reports, a homemade programmable slide-coating system is used to deposit the functional layers to ensure the reproducibility of the fabrication process. The FOSCs are prepared with the similar device architectures of our early works (Fig. 1a)[7,22]. Considering the industrial scalability of the FOSC manufacturing process, the low-cost industry-grade commercial stainless-steel wire with good flexibility and tenacity is selected to replace the expensive laboratory-grade stainless-steel wire to act as the substrate and core electrode. The functional layers of FOSC are sequentially coated onto the surface of the pre-cleaned steel wire by layer. The electron transport layer (ETL) is first coated on the steel wire, followed by the ternary active layer and hole transport layer (HTL). The highly conductive CNT yarn twines around the primary electrode to complete the fabrication of the FOSCs. As illustrated in Fig. 1, (N, N-dimethyl-ammonium N-oxide) propyl perylene diimide (PDINO) with high electron affinities is acted as the ETL[23], the NFA-based ternary organic semiconductor blend of PM6:Y6:$PC_{71}BM$ is adopted as the light absorption layer (Supplementary Fig. 1)[19,24], and the conjugated polymer PEDOT:PSS (AL4083 and PH1000) is used as the HTL and transparent electrode to help the contact between the primary electrode and the counter electrode.

The flexible CNT yarn as the counter electrode is closely twined around the primary electrode with suitable tightness to ensure good contact with HTL and meanwhile avoid damage to the bottom layers. With the homemade slide-coating system, the FOSC devices can be prepared with a length of over one meter. The photograph of the primary electrode in Fig. 1c–g shows that the as-prepared primary electrode looks as thin as the stainless-steel wire substrate. Since the industry-grade commercial stainless-steel wire is used as the core electrode in this study, the surface of the wire is much rougher than the lab-grade wire (Fig. 1b). Even after the functional layers are deposited, the surface of the primary electrode is still maintaining the rough state due to the functional layers are too thin to flatten the uneven surface (Fig. 2a). However, the functional layers can homogeneously cover the wire surface and form a continuous and homogeneous film (Supplementary Fig. 2).

To evaluate the morphology details of the multiple coated layers, the scanning electron microscope (SEM) characterization is carried out (Supplementary Fig. 2). After the PDINO layer is coated, the wire is fully covered with the PDINO layer, and the film surface becomes more homogeneous and smoother than the bare wire. The SEM image with higher magnification indicates that the PDINO layer is compact with few defects (Supplementary Fig. 2a). The high-quality compact ETL layer is crucial for the coating of upper layers including the active layer and HTL layers, and it also helps the device performance by suppressing the charge recombination which we will discuss in the device performance characterization section later. After the active layer and HTL layers are deposited, the primary wire is covered with a homogeneous multilayers film and formed a smoother surface (Supplementary Fig. 2b–d). The cross-section samples were prepared through the multi-column Helium ion microscope and focused ion beam (HIM-FIB) system (Supplementary Fig. 3), and the Pt protection layer was deposited on the top layer to alleviate the damage of the polymer materials. The cross-section SEM image shows that the functional layers are tightly stacked layer by layer (Fig. 2c). The thickness of

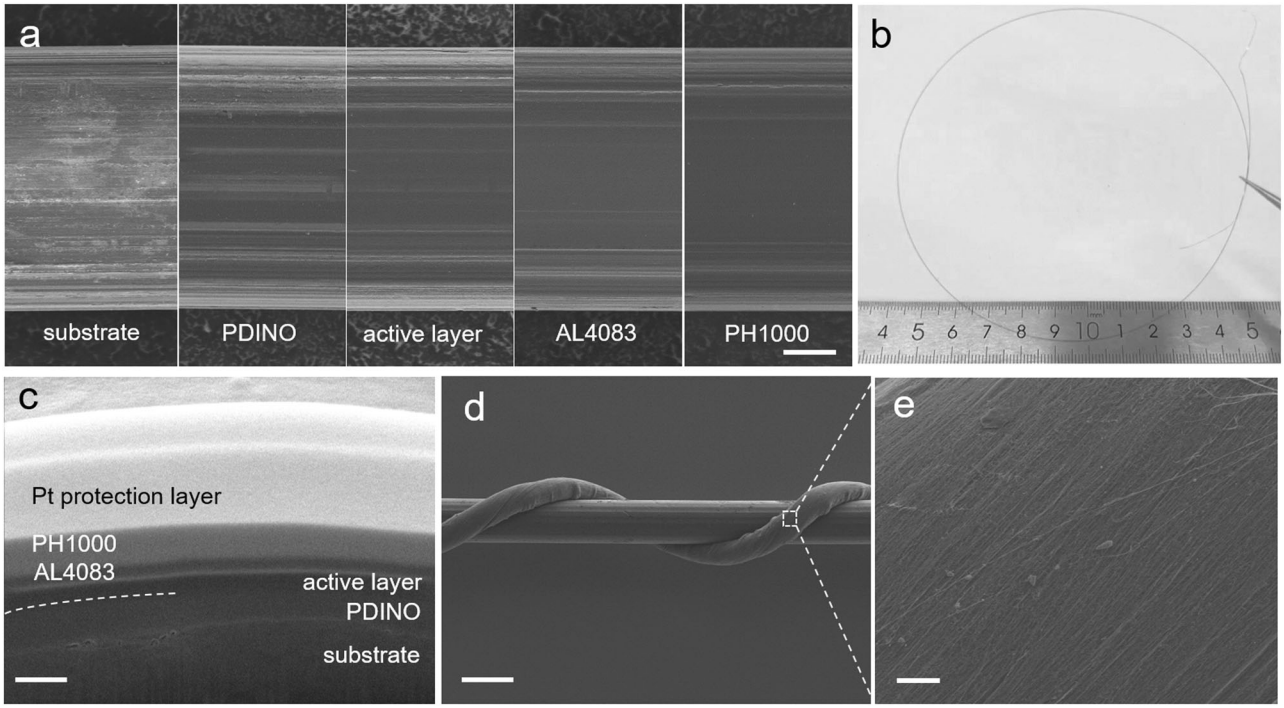

Fig. 2 Characterization of the functional materials for FOSCs. a Surface morphology of each function layer. **b** Full view image and **c** cross-sectional SEM image of the multi-layer film coated on primary electrode. **d** SEM image of the complete FOSC device. **e** Enlarged view of the CNT yarn counter electrode. The scale bars are 20 μm, 300 nm, 100 μm, and 5 μm in **a**, **c**, **d**, and **e**, respectively.

PDINO layer, ternary active layer, and PH1000 layer is about 200 nm, 110 nm, and 250 nm, respectively. The thickness of each functional layer is slightly fluctuated along the axial direction and from batch to batch, which can be roughly controlled in a certain range when the fabrication condition is fixed (Supplementary Fig. 4). The photograph of the complete FOSC device shows that the flexible CNT yarn tightly twines around the primary electrode, and no gap is found between the CNT yarn and the primary electrode (Fig. 2d). Good electrical contact is one of the key parameters to obtain high device performance for FOSCs.

Photovoltaic performance of FOSCs

In order to obtain the best photovoltaic performance, the fabrication conditions including the thickness of multiple layers and the pitch of surrounding counter electrodes are systematically optimized (Supplementary Fig. 5). Since the ETL layer is located at the bottom of the primary electrode, its morphology can obviously influent the upper layers and accordingly affect the device performance, the thickness and morphology of PDINO layer are studied first. The PDINO solutions with the concentration from 20 mg/mL to 50 mg/mL are used to prepare the ETL with various thicknesses. The photovoltaic performance of FOSCs is then characterized under AM 1.5 G standard illumination conditions. The result shows that the device prepared with 40 mg/mL PDINO solution has the best performance with an open-circuit voltage (V_{OC}) of 0.592 V, a short-circuit current density (J_{SC}) of 22.4 mA/cm^2, a fill factor (FF) of 49.6%, a power conversion efficiency (PCE) of 6.58%, and an average PCE of 6.15±0.47% (Supplementary Fig. 5a and Supplementary Table 1). We performed the SEM characterization to investigate the effects of PDINO layers on device performance (Supplementary Fig. 6). The SEM images indicate that the PDINO layer prepared by the solution with the concentration of 20 mg/mL cannot fully cover the surface of the steel wire. The uncovered steel wire surface may make direct contact between the core electrode and the ternary active layer which will increase the charge recombination and result in high current leakage. By contrast, the device prepared with 40 mg/ml solution exhibits full coverage of the substrate and formed a relative smooth PDINO film (Supplementary Fig. 2a, Supplementary Fig. 6c). The ETL with reasonable thickness can not only effectively transport the electrons from the active layer to the electrode, but also decrease the current leakage by fully covering the surface of the core electrode.

Owing to the thickness of active layer is the key parameter for OPV devices, the thickness-dependent study of our FOSCs for the active layer is also carried out during the optimization procedure. As shown in Supplementary Fig. 5b and Supplementary Table 2, the device prepared with 24 mg/mL organic semiconductor blend solution presents the highest device efficiency of 5.90% with a higher V_{OC} of 0.615 V, a J_{SC} of 22.7 mA/cm^2, and an FF of 42.2%, and the average device efficiency collected from 10 different devices is 5.55 ± 0.37%. The device with 16 mg/mL blend solution shows the lowest V_{OC} and J_{SC} of only 0.513 V and 19.6 mA/cm^2, respectively, thus resulting the lowest PCE of only 4.69% with an average PCE of 3.86±0.54%. We infer that the active layer is too thin to sufficiently absorb the photons, and result in the low photocurrent. In addition, the devices with the thin or thick active layer are easy to cause charge recombination, which is not beneficial to improving the performance of the devices. Similar to ETL, the thickness of HTL is also optimized in the study (Supplementary Fig. 5c). The dark current of the FOSCs devices was tested and the diode ideality factor was determined to decrease from 7.54 to 2.09 as the HTL layer increased from 0 to 4 layers, and further increasing the layers of PH1000 cannot show the benefit to the ideality factor (Supplementary Fig. 7a). Thus, the thicker HTL of about 250 nm is necessary for the FOSCs to suppress the charge recombination. Notably, we found that a thin low conductive PEDOT:PSS (AL4083) layer insert between the active layer and the highly conductive PH1000 layer can dramatically enhance the device fill factor (Supplementary Fig. 5d). We infer that the charge recombination can be further suppressed by the AL4083 layer. The diode ideality factor of the solar cell devices was determined from the dark *I-V* curves

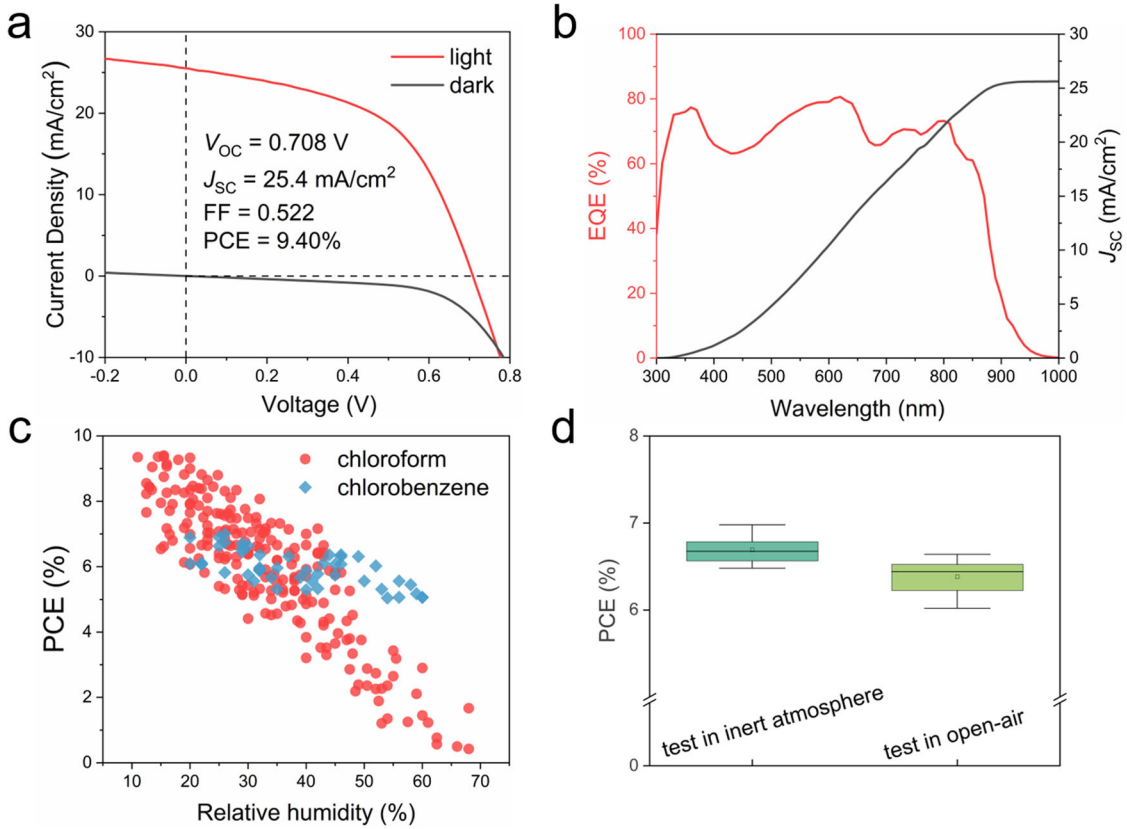

Fig. 3 Photovoltaic performance of the FOSCs. a *J–V* curves of the champion FOSC device (irradiation length, 5 mm), prepared under 10–15% relative humidity. **b** External quantum efficiency of the device and the calculated J_{SC}. **c** Statistic PCE of the FOSCs obtained under different room humidity conditions. Chloroform and chlorobenzene are used as the solvent for the organic photovoltaic materials. **d** Statistical device efficiencies of the FOSCs (prepared under 42-45% relative humidity) tested in open-air and inert atmosphere conditions, the median line and mean value are included in the box-plot.

(Supplementary Fig. 7b), which is always at a high level of more than 5 for the FOSCs without AL4083, suggesting that either bulk or surface recombination through defects states is limiting the performance of the devices. After the introducing of the low conductive AL4083 layer, the diode ideality factor decreased from 8.77 to 2.09, which is well confirmed with our inference that the optimization of interfaces is possible to limit the recombination pathways and further enhance the device performance.

It is easy to understand that the pitch of the counter electrode is an important factor for the device efficiency. On the one hand, the small pitch can help the contact between the primary electrode and the counter electrode in our dual-axis electrode structure, which helps the device performance. On the other hand, the small pitch will present the larger light shading area by the opaque counter electrode which can decrease the light current. A suitable pitch of the counter electrode is needed for the dual-axis FOSCs. Therefore, the influence of counter electrode pitches on device performance is then tested. The device with the counter electrode pitch of 0.7 mm shows the highest FF of 53.1%, with the moderate V_{OC} of 0.628 V and J_{SC} of 22.9 mA/cm^2, thus presenting the highest PCE of 7.64% with an average value of 7.25±0.47% (Supplementary Fig. 8 and Supplementary Table 3). However, the device with the smaller and bigger pitches are not shown the significant performance change. The high tolerance of the counter electrode pitches indicates the lower fabrication requirements which help the promotion of its applications.

After systematically optimization, the champion FOSC device can achieve an efficiency of 9.40% with a V_{OC} of 0.708 V, a J_{SC} of 25.4 mA/cm^2, and an FF of 52.5%. The current-voltage (*J-V*) curves of the champion device are shown in Fig. 3a. The external quantum efficiency (EQE) characterization of the device is also performed (Fig. 3b). The integrated EQE gives a J_{SC} of 25.1 mA/cm^2, which is well-matched with the *J-V* measurement value. Based on the space-charge limited current (SCLC) model, the defect density of the FOSCs is calculated to be 6.36×10^{15} cm^{-3}, and the carrier mobility is 2.14×10^{-4} cm^{2}V^{-1}s^{-1} for electron only device and 1.03×10^{-4} cm^{2}V^{-1}s^{-1} for hole only device, respectively (Supplementary Fig. 9). Compared with the planar devices based on the same photoactive material and charge transform materials, the defect density in FOSCs is obvious higher (6.36×10^{15} cm^{-3} for fiber-shaped device, and 3.69×10^{14} cm^{-3} for planar device), which might be caused by the rough surface of the wire substrate, and it is also an important issue to impact the V_{OC} and FF in FOSCs.

Humidity effect on FOSCs device performance

It is worthy to mention that we found the device efficiency presents a huge deviation during the over years study period, even though the device fabrication process can be maintained very well. Since our FOSCs are totally prepared and tested in open-air conditions, the ambient environment is seriously suspected to be the cause of affecting device performance. By recording the environment temperature and air humidity of the device fabrication process, we found that the device efficiency is strongly dependent on the humidity of the ambient atmosphere (Fig. 3c). The low humidity fabrication condition can produce high efficiency, the distribution statistical results of PCEs further confirm the humidity effect on the efficiency of FOSCs (Supplementary Fig. 10). In contrast, the high humidity harms the device performance seriously (Supplementary Fig. 11). Due to the lab temperature is stabilized in the narrow range of 20 °C to 25 °C during the whole

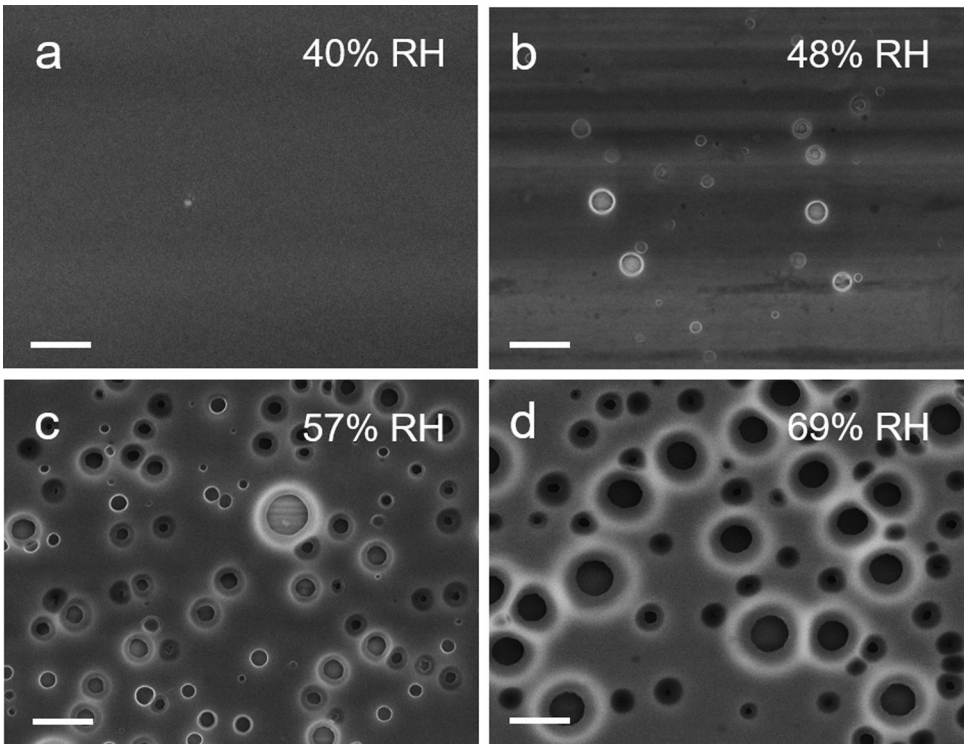

Fig. 4 Effect of humidity on film morphology of the active layer. Film morphology of the PM6:Y6:$PC_{71}BM$ ternary active layer formed under different relative humidity of **a** 40%; **b** 48%; **c** 57%; and **d** 69%, respectively. The scale bar is 1 μm.

year, no obvious relationship between the ambient temperature and the device performance is found (Supplementary Fig. 12).

To further investigate the effect of air humidity on device performance, the SEM characterization of the active layers prepared in the relative humidity (RH) range of 40–69% are performed and analyzed (Fig. 4). Under the 40%-RH condition, the prepared active layer is dense and smooth, no holes are found on the film surface. When the RH increases to 48%, a few holes appear on the film surface. When the RH achieves 69%, plenty of holes are present on the entire film surface, the size of holes even greater than 500 nm. The ETL layer is exposed from the large holes and may contact with the HTL directly, which is suggested to induce charge recombination, thus resulting in inferior photovoltaic performance. To further reveal the effect of fabrication humidity for the FOSCs device performance, the ideality factor of the devices was systematically tested and analyzed (Supplementary Fig. 13a). The ideality factor gradually increased from 2.00 to 10.51 as the ambient humidity increased from 38% to 62%, indicating more charge recombination was happened in the device obtained in higher humidity, and thus resulting in the lower photovoltaic performance. The electrical impedance spectroscopy (EIS) was also applied to determine the charge transfer and recombination, the FOSCs device were measured in the dark at the bias of their respective V_{OC}, as shown in Supplementary Fig. 13b, the Cole–Cole plots exhibit a single semicircle in the complex plane whose diameter is highly dependent on the relative humidity, and the inset gives the equivalent circuit model. When the fabrication humidity is decreased from 62% to 38%, the recombination resistance (R_{rec}) is significantly increased from 2450 to 5880 Ω, indicating less charge recombination in the low-humidity-fabricated devices. These results reveal that the charge recombination is effectively inhibited by reduced defect density, which also correlates to the enhanced device efficiency when the relative humidity decreases.

It is well-known that the solvent can absorb water from the humid air, the precursor solution under high humidity conditions is actually a water-containing solution. To understand the cause of the holes, we added additional water with 5% and 20% volume ratio into the precursor solution and then correspondingly prepared two film samples on the wire substrate. The SEM images show that 5%-water film presents more holes than the control sample, and the holes phenomenon on 20%-water film is more serious than 5%-water film (Supplementary Fig. 14). The result indicates that the water concentration dramatically influences the film morphology. We infer that chloroform with low boiling point volatilized away first during the period of film drying, the water exudes gradually from the precursor and then volatilized away before the film completely dried, and finally formed the holes on the film surface. To further investigate the influence factors of the holes, the influence of the substrate and the species of organic semiconductors was also studied respectively. By removing the PDINO layer, or replacing the PDINO layer with ZnO nanoparticles layer and ZnO nanocrystals layer, the holes are still existing, and the density of the holes has not changed significantly (Supplementary Fig. 15a–c). Similarly, when we replace the NFA-based semiconductor blend with fullerene-based semiconductor blend, the phenomenon of holes on the film surface is still no significant change (Supplementary Fig. 15d). The above analysis indicates that the holes do not clearly relate to the substrate and species of organic semiconductors.

Base on the above study, the low humidity atmosphere condition is suggested to prepare the efficient FOSCs. In addition, as a typical solvent, chlorobenzene with lower water absorption capability and higher boiling point is also introduced to work as the solvent to replace chloroform under high humidity conditions. No holes are found on the surface of chlorobenzene-based precursor films, even under high humidity atmosphere (Supplementary Fig. 16). The device efficiencies prepared with chlorobenzene solvent are recorded in Fig. 3c. The result clearly indicates that the chlorobenzene-based devices show better humidity tolerance, and the obtained devices even can achieve the efficiency of exceeding 5% under the RH of ~60% condition.

Thus, chlorobenzene is also a good candidate to prepare efficient FOSCs, especially, under the high-humidity fabrication atmosphere conditions. However, the solvent is also an important factor to influence the device performance of OPVs, which determines the crystal packing and morphology of organic active layers[25]. The devices prepared with chloroform solvent still show improved performance than chlorobenzene solvent under low humidity conditions.

The photovoltaic performance of FOSCs tested in open-air and inert atmosphere conditions is subsequently compared to further evaluate the effect of humidity on performance measurement. Over 10 FOSC devices fabricated under RH of 42–45% show the average efficiency of 6.41 ± 0.20% and 6.69 ± 0.16% when tested in open-air and inert atmosphere conditions, respectively (Fig. 3d). The efficiency tested in an inert atmosphere is slightly higher than the one tested in open-air conditions due to the slight improvement of FF (Supplementary Fig. 17). However, the other parameters including V_{OC} and J_{SC} are still comparable. The results indicate that the device's performance shows the high tolerance in humid atmosphere. Once the fabrication process is completed, the device performance will not influent a lot by the testing environment.

Detailed performance characterization of FOSCs

To expand the material selection range of the FOSC devices, the ZnO nanoparticles and nanocrystals are introduced to replace the PDINO and acted as the ETL (Supplementary Fig. 18). The comparable performance indicates that ZnO nanoparticles and nanocrystals are the two selectable ETL materials for our FOSCs. Furthermore, as the active layer choices, the PM6:Y6 binary blend is also evaluated and compared with the PM6:Y6:$PC_{71}BM$ ternary blend in the FOSC devices. Both devices prepared with binary and ternary blends present high photovoltaic performance (the PCE is 6.96% for binary device with a V_{OC} of 0.604 V, a J_{SC} of 23.0 mA/cm^2, an FF of 50.1%, and an average PCE of 6.66±0.37%; the PCE is 7.24% for ternary device with a V_{OC} of 0.611 V, a J_{SC} of 23.9 mA/cm^2, an FF of 49.7%, and an average PCE of 6.85±0.44%), while the device with ternary blend active layer shows the higher J_{SC} (Supplementary Fig. 19a and Supplementary Table 4). The EQE characterization indicates that the third component of $PC_{71}BM$ gives the contribution to the increasing of EQE at the shorter wavelength and resulting in the enhancement of J_{SC} and PCE (Supplementary Fig. 19b). The observation is in good agreement with the previous reports in planar structured ternary OPVs[24].

The detailed characterizations of device performance such as flexibility, uniformity, and stability are then successively carried out. Since both the primary electrode and counter electrode have excellent flexibility, the prepared FOSCs also show good flexible capability. The device performance can maintain very well during the period of bending the FOSCs to more than 90 degrees (Supplementary Fig. 20a). The good flexibility makes the FOSC devices expected to be used in applications such as textiles, clothing, and tents, etc. The radial uniformity of the device is then tested. The typical photovoltaic parameters of the FOSC device during the rotation process are recorded in Supplementary Fig. 20b. The device performance can be well-maintained when the device is rolled around the axis. The small fluctuation of the parameters indicates that good radial uniformity of the FOSCs and the device performance is independent of the light illumination angle. Due to the advantages of the FOSCs on 360°-light-harvesting capability, the output power of the fiber device could be significantly enhanced with the utilization of a reflector (Supplementary Fig. 20c). By absorbing the diffuse light from the back-side of the active layer, the output power of the device can even double from the normal illumination (Supplementary Fig. 20d). The output power enhancement is mainly caused by the increased I_{SC}. The FOSC with the length of 5 cm is tested to evaluate the axial uniformity of the device. As shown in Supplementary Fig. 21a, the efficiencies of the device are recorded with the interval length of 1 cm. Each part of the device shows a close PCE value of 6.5–7%. The efficiency deviation as small as 0.34% suggests the device performance has good uniformity along the axial direction.

When increasing the irradiation length from 1 cm to 5 cm, the irradiation active area multiple increases from 0.01 cm^2 to 0.05 cm^2, and the generated photocurrent of the FOSC increases from 0.23 mA to 0.61 mA, while the calculated photocurrent density is 22.6 mA/cm^2 for 1 cm device and 12.3 mA/cm^2 for 5 cm device, which is conjectured to be mainly caused by the increased internal resistance of the fiber device (Fig. 5a). This phenomenon is consistent with the results reported in fiber-shaped DSSCs[26]. We further increase the irradiation length to 16 cm to monitor the device working status. The long FOSC maintains a good working status and finally outputs the working power of 0.40 mW (Supplementary Fig. 21b). The milliwatt-grade power output makes the FOSCs closer to the applications on microelectronic devices. However, the power generated from the single FOSC is still limited and it is hard to obtain sufficient output power by simply increasing the length of a single device. Combining multiple FOSCs in series or parallel can significantly increase the output power. As shown in Fig. 5b, the single device presenting a V_{OC} of 0.611 V, and a J_{SC} of 0.122 mA. With series connection, the I_{SC} maintains the value of about 0.12 mA, while the V_{OC} multiply increased from 0.611 V to 1.24 V, 1.84 V, and 2.44 V when series connect with 1–3 additional FOSC devices. In the configuration of paralleling, each device delivers the voltage of about 0.6 V, the multiple increased I_{SC} of 0.122 mA, 0.250 mA, 0.379 mA, and 0.504 mA were achieved, respectively (Fig. 5c). The voltage and current increase regularly with the number of series or parallel connections, which indicates that connecting FOSC devices in series and parallel is an effective strategy for preparing smart textile devices with considerable energy supply (Fig. 5d).

Application of FOSCs in wearable devices

To further expand the application possibilities of FOSCs, we utilize the cheap commercial Ag wire to replace the CNT yarns to act as the counter electrode. The thin Ag wire with a diameter of 25 μm shows good flexibility and high conductivity. The comparable photovoltaic performance of Ag wire-based FOSC suggests that the Ag wire is a suitable substitute counter electrode material for the CNT yarns (Supplementary Fig. 22). With the Ag wire counter electrode, we carried out several application attempts on our FOSCs, such as the FOSC bundle or textile drives the mini-fan and the red light-emitting diode (LED) (Supplementary Video 1–6). More than 3 mA constant photocurrent can be obtained by paralleling 6 FOSCs (irradiation length: 3 cm). As shown in the video S1, the mini-fan (startup current: 2.8 mA) can be continuously driven under the illimitation of outdoor sunlight. By exposing the FOSCs to sunlight from the cover of shadow, the originated current of FOSCs can quickly respond to the sunlight, where the fan immediately returns to the work state from the static state. As shown in Supplementary Fig. 23, the red LED lamp (startup voltage: 2.8 V) can be successfully lighted since the 6 FOSCs in series connection can achieve over 3.0 V voltage under the light illumination.

Since the flexible FOSCs are fabricated with thin wire electrodes where the wire diameters are only 0.1 mm or less, the FOSCs can be easily weaved into the textiles (Supplementary Fig. 24). To protect the functional layers and fix the position of the counter electrode when weaving the FOSCs into the textiles, the FOSCs were simply encapsulated by the general-purpose instant adhesive. The *J–V* characterization indicates that the device performance is well-maintained (Supplementary Fig. 25). Interestingly, the encapsulated FOSCs present the good waterproof

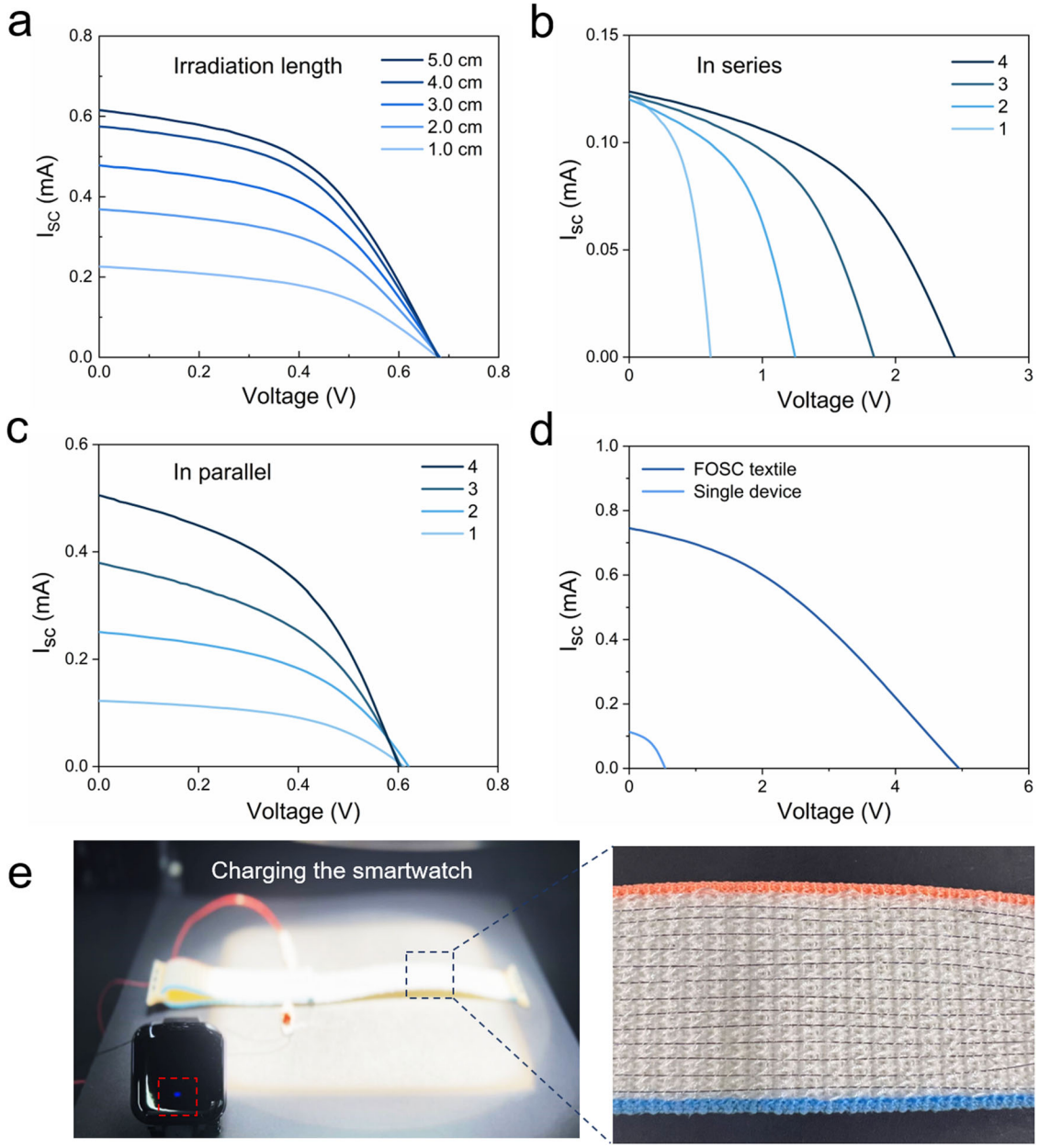

Fig. 5 FOSCs connected in series or parallel to enhance the output power. Photovoltaic performance of the FOSCs **a** varying in irradiation length, **b** connected in series, and **c** connected in parallel. **d** Photovoltaic performance of the wearable textile weaved with FOSCs. **e** The watchband weaved with the FOSCs used to charge the smartwatch.

property (Supplementary Video 2). The robust performance and the waterproof properties make the FOSC a good candidate to the photovoltaic textiles. The weaved FOSCs in the textile also can drive the mini-fan under the light illumination and exhibit a good power conversion capability (Supplementary Video 3). By virtue of the unique 1D architecture of the FOSCs, the textiles weaved by the FOSCs are available on both sides, which can generate power and supply energy from both sides of the reversible textile (Supplementary Video 4). We also tried to apply these FOSC devices in wearable electronic devices as the energy supply source. As shown in Fig. 5e, the FOSCs are successfully weaved with the watchband. Under the light illumination, the watchband can provide sufficient output power (>5 V, 0.7 mA) to charge the smartwatch (Supplementary Video 5). By virtue of the superior flexibility, the FOSC knitted watchband maintain stable and robust photovoltaic performance even after continuous bending and twisting (Supplementary Video 6). Above attempts of FOSC devices on driving the electrical appliances show the great application potential of FOSCs in wearable devices and smart textile applications.

The long-term stability of FOSCs is also monitored in open-air conditions (Supplementary Fig. 26). After one week of storage in open-air atmosphere, the efficiency of the unencapsulated device drops from 9.4% to 5.28%. The device efficiency gradually degrades to 3.16% after one month of storage and 1.38% after two months of storage, respectively. Though the efficiency drops a lot, the result is still encouraged since the bare device has not been added to any protection and encapsulation. With simple encapsulation, the device stability is obviously improved compared with the FOSC device without encapsulation, and the efficiency can maintain ~50% after 2 months of storage in open-air. The slowly degraded efficiency of the encapsulated FOSCs

devices indicates that physical encapsulation is an effective approach to improve the stability of FOSCs.

CONCLUSIONS

Due to the unique advantages, such as the 1D conformation and weave-ability, the fiber-shaped optoelectronic devices demonstrate broad application prospects in wearable devices and the smart textile field[27]. Improving the device performance, developing the large-scale processing technology, and expanding the scope of application are still the main directions of effort for the research. In this study, we demonstrate efficient FOSC devices with NFA-based light-harvesting materials. The low-cost industry-grade wires, such as the stainless-steel wire and silver wire, are used as the electrodes which expand the applicable occasions on the practical applications. All the preparation processes are carried out in open-air conditions. The fabrication process is assisted by a programmed slide-coating system which can provide a reference for the scale-up production. By systematically investigated each functional layer of the primary electrode, the structure of FOSC can be well understood and optimized. The prepared FOSCs present a PCE of up to 9.40% which is among the highest efficiency for FOSC to date (Supplementary Fig. 27). The humidity is suggested as the key factor that affects the device performance during the fabrication process. The suitable solvents are suggested to fabricate the efficient FOSCs under different humidity atmosphere conditions. By connecting multiple devices in parallel or series, the FOSCs show the considerable energy supply capability for the low-electricity-consumption devices, which indicates that the FOSCs are promising for practical applications. Importantly, the initial attempt of charging smart devices by FOSCs indicates the great potential of FOSCs to be applied in practical wearable electronics. This work not only provides an effective approach to preparing the efficient FOSCs but also shows a good instance to apply the FOSCs as the energy supply of wearable electronic devices and smart textile applications.

METHODS

Chemicals and materials

(N,N-dimethyl-ammonium N-oxide) propyl perylene diimide (PDINO), PM6, Y6, and $PC_{71}BM$ were purchased from Organtec Ltd, Beijing. Two types of PEDOT:PSS (AL4083 and PH1000) were purchased from Heraeus Inc., Germany. 1-chloronaphthalene was purchased from TCI Co., Ltd, Shanghai. Methanol was purchased from Alfa Aesar Ltd, Shanghai. Chloroform and chlorobenzene and other solvents were acquired from J&K Chemicals Inc. The stainless-steel wire (316 grade, diameter of 100 μm) was purchased from Wanwei Stainless Technology Co., Ltd. Ag wire (diameter of 25 μm) was purchased from Juyuan Silver Material Co., Ltd. CNT wire (40–60 μm), ZnO nanoparticles, and ZnO nanocrystals were prepared according to the literature procedures, respectively[7,28]. The general-purpose instant adhesive (Kafuter-502) used for encapsulation was purchased from Kafuter Co., Ltd.

General design of the slide-coating system

The fabrication process of the FOSCs is taken by a simple homemade slide-coating system. The industrial-grade stainless-steel wire is used as the substrate and the axial electrode. The programmable logic controller was applied to the stepping motor, which drives to numerically control the slide unit. The moving speed of the slide unit can be adjusted from 100 mm/min to 5000 mm/min. A pipette with a tip-head was fixed to the slide unit, where solution droplets can be generated when the pipette tip is full of solution. The diameter of the precursor solution droplet is controlled to 2–3 mm which is larger than the diameter of the primary steel wire so that the steel wire can be completely immersed into the precursor droplet along the radial direction. The coating is homogeneously deposited after the droplet going through. The continuous and scalable coating can be achieved via this system. The functional coating layer with various layer thicknesses can be obtained by adjusting solution concentration, coating speed, and coating cycles.

Preparation of fiber-shaped solar cells

The stainless-steel wire was sequentially cleaned with soap water, acetone, and ethanol. The methanol-dissolved PDINO solution was first dip-coated with the coating speed of 5000 mm/min to act as the ETL. The active layer material of PM6:Y6:$PC_{71}BM$ mixed in the weight ratio of 1:1:0.2 was dissolved in chloroform with the additive of 1-chloronaphthalene (0.5%, v/v). With the same coating procedure, the wire was secondly coated with the active layer. The PEDOT:PSS layers, including AL4083 layer and PH1000 layer were sequentially deposited upon the active layer with the coating speed of 1000 mm/min. The coating procedure for the PH1000 layer was repeated multiple cycles to increase the layer thickness. Then the coated steel wire was annealed at 140 °C for 4 min in air. Finally, the counter electrode of CNT wire or Ag wire was wrapped around the primary electrode to form the physical and electrical contact. For the encapsulated devices, the adhesive was coated on the FOSCs via the same coating procedure of the functional layers, and the coating speed was adjusted to 1000 mm/min, the procedure was adequately repeated 3 times and dried for about 3 min to form a full encapsulation.

Characterization of fiber-shaped solar cells

The surface morphology of the function layer was observed by field emission scanning electron microscope (SEM, Zeiss, Gemini500). The in-suit milling and imaging of the FOSCs was obtained through the multi-column Helium Ion Microscope and Focused Ion Beam system (HIM-FIB, Zeiss, ORION NanoFab). Before milling, a Pt protect layer was deposited on the top layer to alleviate the damage to the polymer materials. The photovoltaic performance of the fiber-shaped solar cells was characterized by a Keithley 2400 semiconductor characterization system and illuminated by an oriel 450 W calibrated solar simulator (Newport, SP94043A-SR1) with an irradiance of 100 mW/cm^2 at AM 1.5 G where the light intensity was measured using a NREL-calibrated Si reference cell (xenon arc lamp with the spectral-mismatch factor of 1.03 for the devices studied). Devices were scanned at a rate of 50 mV/s with dwell time of 30 ms. The testing area was determined as the illumination length multiplied by the diameter of the primary electrode, where the illumination length can be preciously controlled by a customized mask upon the device. For the diffusing mode, a printer paper was used as the diffuse reflector to put underneath the device during testing. The devices were tested without encapsulation unless otherwise specified. The external quantum efficiency of the fiber-shaped solar cells was determined in the air by a fully integrated EQE characterization system (Newport, Quantx-300).

Ideality factor calculation

The ideality factor (n) is derived from the slope of the dark *I*–*V* curve, and the basic cell equation in the dark is:

$$I = I_0\left(exp\left(\frac{qV}{nkT}\right) - 1\right) \quad (1)$$

where *I* is the current through the diode, *V* is the voltage across the diode, I_0 is the dark saturation current, T is the temperature in kelvin, q and k is the elementary charge constant and Boltzmann constant.

Taking the log of both sides of the equation gives:

$$ln(I) = ln(I_0) + \frac{qV}{nkT} \quad (2)$$

and when plotting the natural log of the current against the voltage, the slope will be determined and the ideality factor can be calculated from the following equation:

$$slope = \frac{q}{nkT} \quad (3)$$

Defect density and carrier mobility calculation

Based on the space-charge limited current (SCLC) model, the defect density and the carrier mobility of the device can be obtained. We can obtain the trap filled limit voltage V_{TFL} from the kink point in the dark *J*–*V* plots. The trap density (N_t) can be calculated as the following equation:

$$N_t = \frac{2\varepsilon\varepsilon_0 V_{TFL}}{eL^2} \quad (4)$$

where ε_0 is the vacuum permittivity, and ε is assumed to be 30 for the organic material, e is the elementary charge, L is the thickness of the active layer film.

Also, the carrier mobility (μ) can be calculated as the following equation:

$$\mu = \frac{8L^3 J}{9\varepsilon\varepsilon_0 V^2} \quad (5)$$

where the electron mobility can be obtained based on the ETL only device with the structure of stainless-steel wire/ZnO/active layer/PDINO/CNT wire, and the hole mobility can be determined from the HTL only device with the device structure of stainless-steel wire/PEDOT:PSS/active layer/PEDOT:PSS/CNT wire.

DATA AVAILABILITY

The experimental data referenced in this manuscript are available upon request to the corresponding author, D.Y.L.

Received: 21 January 2022; Accepted: 10 May 2022;
Published online: 07 June 2022

REFERENCES

1. Sun, H., Zhang, Y., Zhang, J., Sun, X. & Peng, H. Energy harvesting and storage in 1D devices. *Nat. Rev. Mater.* **2**, 17023 (2017).
2. Wang, L. et al. Application challenges in fiber and textile electronics. *Adv. Mater.* **32**, 1901971 (2020).
3. Fan, X. et al. Fibrous flexible solid-type dye-sensitized solar cells without transparent conducting oxide. *Appl. Phys. Lett.* **92**, 113510 (2008).
4. Chen, T., Qiu, L., Kia, H. G., Yang, Z. & Peng, H. Designing aligned inorganic nanotubes at the electrode interface: towards highly efficient photovoltaic wires. *Adv. Mater.* **24**, 4623–4628 (2012).
5. Liu, J., Namboothiry, M. A. G. & Carroll, D. L. Optical geometries for fiber-based organic photovoltaics. *Appl. Phys. Lett.* **90**, 133515 (2007).
6. Lee, M. R. et al. Solar power wires based on organic photovoltaic materials. *Science* **324**, 232–235 (2009).
7. Liu, D. et al. Solid-state, polymer-based fiber solar cells with carbon nanotube electrodes. *ACS Nano* **6**, 11027–11034 (2012).
8. Qiu, L., Deng, J., Lu, X., Yang, Z. & Peng, H. Integrating perovskite solar cells into a flexible fiber. *Angew. Chem. Int. Ed.* **53**, 10425–10428 (2014).
9. Li, R., Xiang, X., Tong, X., Zou, J. & Li, Q. Wearable double-twisted fibrous perovskite solar cell. *Adv. Mater.* **27**, 3831–3835 (2015).
10. Qiu, L., He, S., Yang, J., Deng, J. & Peng, H. Fiber-shaped perovskite solar cells with high power conversion efficiency. *Small* **12**, 2419–2424 (2016).
11. Sangiorgi, N. et al. Improving the efficiency of thin-film fiber-shaped dye-sensitized solar cells by using organic sensitizers. *Sol. Energy Mater. Sol. Cells* **204**, 110209 (2020).
12. Casadio, S. et al. Highly efficient long thin-film fiber-shaped dye sensitized solar cells based on a fully organic sensitizer. *Sol. Energy Mater. Sol. Cells* **224**, 110986 (2021).
13. Fu, X. et al. A fiber-shaped solar cell showing a record power conversion efficiency of 10%. *J. Mater. Chem. A* **6**, 45–51 (2018).
14. Dong, B. et al. High-efficiency fiber-shaped perovskite solar cell by vapor-assisted deposition with a record efficiency of 10.79%. *Adv. Mater. Technol.* **4**, 1900131 (2019).
15. Zhang, Z. et al. Weaving efficient polymer solar cell wires into flexible power textiles. *Adv. Energy Mater.* **4**, 1301750 (2014).
16. Liu, P. et al. Polymer solar cell textiles with interlaced cathode and anode fibers. *J. Mater. Chem. A* **6**, 19947–19953 (2018).
17. Yan, C. et al. Non-fullerene acceptors for organic solar cells. *Nat. Rev. Mater.* **3**, 18003 (2018).
18. Meng, L. et al. Organic and solution-processed tandem solar cells with 17.3% efficiency. *Science* **361**, 1094–1098 (2018).
19. Yuan, J. et al. Single-junction organic solar cell with over 15% efficiency using fused-ring acceptor with electron-deficient core. *Joule* **3**, 1140–1151 (2019).
20. Zhang, M. et al. Single-layered organic photovoltaics with double cascading charge transport pathways: 18% efficiencies. *Nat. Commun.* **12**, 309–318 (2021).
21. Bi, P. et al. Reduced non-radiative charge recombination enables organic photovoltaic cell approaching 19% efficiency. *Joule* **5**, 1–12 (2021).
22. Liu, D. et al. Single-layer graphene sheets as counter electrodes for fiber-shaped polymer solar cells. *RSC Adv.* **3**, 13720–13727 (2013).
23. Zhang, Z.-G. et al. Perylene diimides: a thickness-insensitive cathode interlayer for high performance polymer solar cells. *Energy Environ. Sci.* **7**, 1966–1973 (2014).
24. Yan, T. et al. 16.67% rigid and 14.06% fexible organic solar cells enabled by ternary heterojunction strategy. *Adv. Mater.* **31**, 1902210 (2019).
25. Zhu, L. et al. Efficient organic solar cell with 16.88% efficiency enabled by refined acceptor crystallization and morphology with improved charge transfer and transport properties. *Adv. Energy Mater.* **10**, 1904234 (2020).
26. Liu, Z. & Misra, M. Dye-sensitized photovoltaic wires using highly ordered TiO_2 nanotube arrays. *ACS Nano* **4**, 2196–2200 (2010).
27. Shi, X. et al. Large-area display textiles integrated with functional systems. *Nature* **591**, 240–245 (2021).
28. Liu, D. & Kelly, T. L. Perovskite solar cells with a planar heterojunction structure prepared using room-temperature solution processing techniques. *Nat. Photonics* **8**, 133–138 (2014).

ACKNOWLEDGEMENTS

This work was supported by the Westlake Education Foundation. Y.S. also acknowledges the financial support from the National Natural Science Foundation of China (51872267). We thank for the facility support and technical assistance from the Instrumentation and Service Center for Physical Sciences (ISCPS), as well as the Center for Micro/Nano Fabrication at Westlake University.

AUTHOR CONTRIBUTIONS

D.Y.L. conceived the research project. D.Y.L. and D.L. designed the experiments. D.L. carried out the experiments. Y.S. prepared the CNT yarns. Q.J. contributed to the HIM-FIB characterization and the related data analysis. D.Y.L. and D.L. discussed and analyzed the experimental data, and prepared the manuscript. All authors contributed to the manuscript revisions.

COMPETING INTERESTS

D.L. and D.Y.L. have filed a patent application based on the work in this manuscript. Q.J. and Y.S. declare no competing interests.

ADDITIONAL INFORMATION

Supplementary information The online version contains supplementary material available at https://doi.org/10.1038/s41528-022-00172-w.

Correspondence and requests for materials should be addressed to Yuanyuan Shang or Dianyi Liu.

Reprints and permission information is available at http://www.nature.com/reprints

Publisher's note Springer Nature remains neutral with regard to jurisdictional claims in published maps and institutional affiliations.